University of Pisa

Laboratory Report

Aperture Photometry and PSF Fitting Analysis of Vega, Deneb, and the Pleiades

Professors:
Prof. Massimiliano Razzano
Prof. Angelo Ricciardone
Prof. Barbara Patricelli
Prof. Andrea Pallottini

Candidates:
Nicolò Aimone Braida (701844)
Matilde Biscaro (702943)
Lorenzo Nepi (701845)

Academic Year: 2024-2025

22 November. 2024

Abstract

The goal of this laboratory experience is to conduct observations at optical wavelengths and perform photometric measurements using CCD cameras. The first part of the activity will be devoted to the characterization of the electronic camera, while the second one will be dedicated to the photometric measurements of the stars Deneb and Vega, as well as the Pleiades and NGC 869 clusters. We found a calibrations constant of $C = 21.40 \pm 0.07$ for the energy flux - magnitude relation. The final tasks consists in performing Aperture Photometry and PSF Fitting on the detected sources and computing their magnitude. The magnitude of Merope, Alcyone, Maia and Asterope II was evaluate at 4.35 ± 0.11, 3.78 ± 0.09, 4.24 ± 0.10 and 5.32 ± 0.16 respectively, while reliable measurements for NGC 869 could not be obtained because of persistent systematic errors.

Contents

1 Introduction 1

2 Theoretical Background 1
- 2.1 Instrumentation and Observing Set Up . . 2
  - 2.1.1 Telescope 2
  - 2.1.2 CCD 2
  - 2.1.3 Structure 2
  - 2.1.4 Operating Principles 2
- 2.2 Aperture Photometry and PSF Photometry 3
- 2.3 Magnitude 3
- 2.4 Calibration of Astronomical Images 3

3 Observation 4

4 Data Reduction and Results 4
- 4.1 Bias frames 4
- 4.2 Flat-Field frames 5
- 4.3 Dark current frames 5
- 4.4 Gain and Readout Noise 6
- 4.5 Photometry on calibrated images 6
  - 4.5.1 Searching for the calibration constant C 6
  - 4.5.2 Magnitude of stars in the Pleiades cluster 7

5 Discussion 8
- 5.1 CCD characterization problems 8
- 5.2 Image processing issues 8

6 Conclusion 9

A Appendix 9
- A.1 Computing the uncertainty on the counts of each pixel 9
- A.2 Figures 10

References 11

1 Introduction

Photometry is one of the oldest techniques for investigating the sky. The human eye's ability to collect photons actually marked the beginning of the successful history of optical astronomy. This type of investigation is based on the presence of detectors capable of collecting photons coming from a luminous source and estimating their number, in order to determine the intensity of the received radiation. The evolution of astronomical instrumentation for photometry after the human eye itself progressed through the use of photographic plates, and has now reached modern CCDs (Charge-Coupled Devices), silicon-based sensors that collect photon-generated electrons via potential wells (see Sec. 2.1.2).
After having collected photons coming from a certain source through a CCD camera, one can proceed to convert the counts recorded into the most commonly used scale for expressing the brightness of an object, namely the magnitude scale. In this exercise, we observed two stars with known magnitudes (Deneb and Vega) in order to calibrate the conversion from instrumental counts to apparent magnitude. This calibration was then used to compute the magnitudes of other astronomical objects, such as stars in the Pleiades cluster.

2 Theoretical Background

Photometry is a technique that allows us to measure the flux and the magnitude of various sources starting from the quantity of emitted photons detected. To perform a photometric measurement and analysis, a system of instruments is needed: a telescope, to collect the light, several photometric filters, to select particular wavelength ranges and a CCD to record our data. In the following section we will quickly go trough the basic concepts needed for the experience.

2.1 Instrumentation and Observing Set Up

2.1.1 Telescope

The optical telescope used for this experiment is a Celestron C11 Schmidt-Cassegrain Telescope with 280 mm diameter, and a focal ratio of f/10, with the capability of automatic alignment and pointing. The Cassegrain configuration is described in Fig. 1. To set up our telescope,

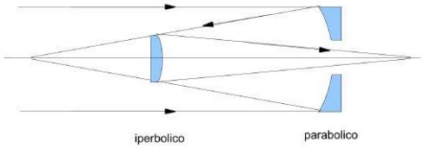

Figure 1: Schematic representation of the configuration of a Cassegrain telescope. The system consists of a perforated, concave, parabolic primary mirror and a convex, hyperbolic secondary mirror. The focal plane is located behind the primary mirror. This optical configuration eliminates spherical aberration and reduces coma, owing to its long effective focal length.

we began by placing the tripod on a stable surface, ensuring it was steady and level using the built-in bubble indicator. Once the tripod was properly positioned, we secured the base disc and carefully installed the equatorial head, aligning its main axis with the celestial North Pole. We then attached the counterweights to balance the setup, followed by mounting the optical tube onto the equatorial head. After verifying the overall balance of the system, we made small adjustments where needed. The eyepiece was then installed, and we proceeded with the star alignment procedure using the hand controller. This involved centering three reference stars: Vega, Deneb, and Capella. It is important to note that if the eyepiece is not correctly aligned with the optical axis of the telescope, the three-star alignment process is likely to fail.

2.1.2 CCD

2.1.3 Structure

A CCD is a chip made of silicon, a semiconductor material, whose surface features a matrix of light-sensitive pixels. The chip is enclosed in a package made of metal, ceramic, or plastic. There are also electrical wires and a series of bond pads positioned around the outline of the chip to allow interaction with external components. Below the pixel matrix, we find the serial register, a row of pixels that is hidden and not exposed to light, and the amplifier chip, which serves to amplify the received signal. The structure is schematized in Figure 2.

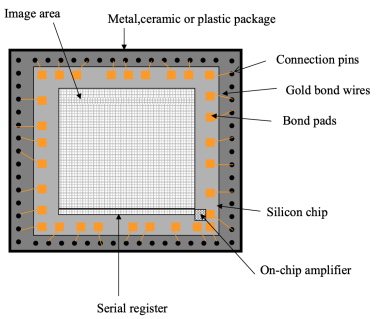

Figure 2: Structure of a CCD. Refer to the labels on the arrows to identify the various components.

Specifically, each pixel has a structure known as a MOS (Metal-Oxide-Semiconductor) capacitor: it consists of a polysilicon electrode, a silicon dioxide insulating layer, an *n-type* silicon layer, and a *p-type* silicon substrate (enriched with electron-accepting atoms), as shown in Figure 3.

Figure 3: Structure of a MOS capacitor. Refer to the labels on the arrows to identify the various components.

Each pixel is equipped with a series of electrodes, called gates, which through the application of specific voltages create potential wells capable of collecting and storing the photo-generated electrons during the exposure. Each pixel typically has three gates, and a different voltage is applied to each gate. At the end of the exposure, the electrons are located in the deepest potential well.

2.1.4 Operating Principles

The CCD operates by exploiting the photoelectric effect, a phenomenon in which electrons are emitted when a photon above a certain frequency limit strikes a metallic surface. Ideally, the number of photons coming from a source can be inferred counting the electrons produced on each pixel. By appropriately modulating the voltages of the pixel electrodes, it is possible to move the electrons from one potential well to another until they reach the serial register, where the information is then processed. The process is illustrated in Figure 4.

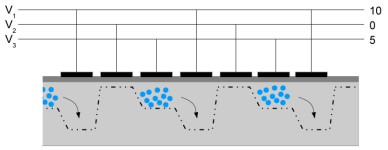

Figure 4: Transfer of charges (represented as blue dots) between the potential wells (represented by the dashed lines).

The output charge is read as a voltage, the signal is amplified, and then converted into an integer number via the analog-to-digital converter (A/D). This integer number is referred to as the *digital number* (DN) or *analog-to-digital unit* (ADU).
The amount of voltage required to produce 1 ADU is called the *gain* (e^-/ADU). In modern CCDs, typical *gain* values range between 1 and 10. The CCD readout process is repeated until the entire matrix of pixels has been read, as soon as all the collected charge has been converted into counts. The reading speed depends on how fast the charge transfer and A/D conversion occur. CCD reading is characterized by the presence of noise, known as *readout noise*, which contributes to the uncertainty associated with the count value of each pixel.
The result of an observation is a matrix whose elements are the number of counts per corresponding pixel.

2.2 Aperture Photometry and PSF Photometry

Photometric observations are often affected by various factors of disturbance. Firstly, atmospheric turbulence significantly degrades the quality of the images for ground-based telescopes. Such effect is generically referred to as *seeing*. Secondly, the telescope may exhibit optical aberrations and be affected by light's interference and diffraction in some of his components. Due to these primary factors, the image of a point-like source (such as a distant star) is distorted into a two-dimensional disk on the focal plane. The Point Spread Function (PSF) describes the response of an imaging system to a point source of light and it represents how the system spreads or blurs the beam due to optical imperfections and atmospheric effects. Mathematically, the PSF is a distribution of luminous flux centered around the direction of the actual source and defined on the focal plane of the telescope (or on the surface of the detector sensor).
PSF photometry techniques consist in estimating the brightness of an object by fitting a model of the PSF over the observed counts and integrating it over the area on the CCD sensor occupied by such object. In doing so, an estimate of the total counts (and therefore of the object luminous flux) is obtained. It is particularly useful in crowded fields such as star clusters or dense galaxies, where sources are close to one another. Note that the background contribution (e.g. sky brightness, light from nearby sources) must be previously subtracted.
Instead, while performing *aperture photometry* one measures the flux from a celestial object by summing the pixel counts within a circular region centered on its image. Since this area includes both the target's light and the surrounding sky, a concentric annular region is used to estimate the background contribution, which is then subtracted.

2.3 Magnitude

The concept of apparent magnitude of a celestial object depends primarily on three factors:

- The object's intrinsic luminosity;
- Its distance from the observer;
- The presence of intervening absorbing or scattering media.

Originally, six classes of apparent magnitude were established through visual photometry using the naked eye or early telescopes. Today, this scale has been refined and extended, with a precise quantitative relationship between magnitude and the amount of light received from an object.
Pogson's Law defines the relationship between the apparent magnitude scale (i.e. the magnitude difference $m_2 - m_1$ between two celestial objects) and the radiant flux I (the amount of energy passing through a unit area per unit time):

$$m_2 - m_1 = 2.5 \log_{10} \left(\frac{I_1}{I_2} \right) \quad . \tag{1}$$

This equation sets the fixed ratio between brightness levels corresponding to a one-magnitude difference.

One can then express the apparent magnitude m of an object of radiant flux I as

$$m = -2.5 \log_{10} (I) + C_m \tag{2}$$

where C_m is a calibration constant. Alternately, the magnitude can be computed directly from observations. Ideally, I is directly proportional to the number of photons per second coming from the source measured by our instruments. Eq. 2 can then be rewritten as

$$m = -2.5 \log_{10} (S - n_{pix} B) + C \tag{3}$$

where S denotes the total counts per unit time recorded in the area of the CCD sensor occupied by the observed object, n_{pix} is the total number of pixels in such area, B is the mean of the background counts per pixel per unit time and C is the calibration constant.
To be more specific, we are considering the *visual* apparent magnitude of an object, since we are only collecting light in the visual frequency band.

2.4 Calibration of Astronomical Images

It is essential to process our images in order to obtain a scientific frame that only shows the contribution of the sources expressed in physical units. In other words, we need to remove the imprint of the instrumentation to compute the actual observed flux. The intensity value in pixel counts of each image contains information from the object and/or the sky, readout noise, dark current (thermally produced electrons), and potential cosmic rays. Moreover, the response of each pixel to light reception is not perfectly identical; therefore, it is necessary to remove this non-uniformity using so-called flat-field frames.
The resulting image can be modeled by a function $ADU(x, y)$ (where (x, y) represents the position of the pixel in the sensor matrix), which ideally expresses the counts coming exclusively from the sources and from the background. Eq. 4 sums up the image calibration process:

$$ADU(x, y) = \frac{[I(x, y) - BIAS(x, y) - DARK(x, y)]}{FF(x, y)} \quad . \tag{4}$$

- $I(x, y)$ represents the "raw" counts observed on the CCD sensor. Basically, $I(x, y)$ is the output of the camera.
- $BIAS(x, y)$ provides the average zero-level of the signal and allows an estimation of the CCD readout noise (see Eq. 6). When the average number of photoelectrons is particularly low, after A/D conversion some pixels may register negative count values, which cannot be represented by the ADC. To prevent this issue, a bias voltage is applied to all pixels, effectively shifting the signal above zero. Before the observations, *bias frames* are acquired with a nominal exposure time of 0 seconds (which means that they can only contain counts coming from the bias level) and must then be subtracted from the science images (as in Eq. 4) during processing.
- $DARK(x, y)$ describes the *dark current* produced in the CCD: due to thermal excitation, some electrons may be produced on the sensor disturbing the

signal. *Dark frames* are acquired by closing the telescope's aperture to prevent any incident photons, thereby eliminating photoelectron emission. In this configuration, the only electrons detected by the CCD are those generated thermally. Dark frames are typically taken with the same exposure time as the corresponding science images (from which they must be subtracted, as in Eq. 4), in order to accurately model the thermal noise contribution.

- $FF(x, y)$ (Flat-Field) accounts for the varying sensitivity of the CCD across its surface. Since not all pixels respond equally to incoming light, flat-field images are taken under uniform illumination to map these variations. The bias and dark-subtracted science image is then corrected by dividing it by the normalized (i.e. divided by its mean) flat frame (Eq. 4).

This shows how, in addition to the targeted sources, during an observation it is mandatory to collect bias, dark current, and flat-field frames.
The process of data reduction (Sec. 4) then involves the characterization of the CCD, in order to subtract the bias and the dark current from the image, the correction for flat-field effects and possibly the filtering out cosmic ray signals (as explained in Sec. 4). Finally, photometric analysis of the resulting image is needed to convert the measurement in physical units.

3 Observation

The telescope model and set-up is described in Sec. 2.1. In addition, we employed a CCD camera ATIK 460 EX monochromatic observing in the visual band. Tab. 1 shows the main characteristics of the camera.

Specification	**Value**
Horizontal Resolution	2750 pixels
Vertical Resolution	2200 pixels
Pixel Size	4.54 μm x 4.54 μm
Sensor Size	12.5 mm x 10 mm
ADC (Analog-to-Digital Converter)	16 bit
Binning	2x2
Readout Noise	5
Power Supply	12V
Maximum Exposure Time	Unlimited
Minimum Exposure Time	1/1000 s
Cooling	Yes ($\Delta T = -25°C$)
Backfocus Distance	13 mm
Telescope Connection	T-thread Female (42x0.75)
Weight	400 g

Table 1: CCD camera ATIK 460EX specifications.

Observations were carried out on 2024-11-22 at 20:00 UTC, from Pisa, Italy. After aligning the telescope (Sec. 2.1) we proceeded as follows:

- The CCD camera was turned on and left to (automatically) cool for about ten minutes. This operation is crucial to reduce thermal noise.
- Bias frames (14 in total) were taken with an exposure time of nearly 0 s (theoretically 0 s, but in practice 0.001 s), with the CCD camera covered and still disconnected from the telescope. The frames were digitally saved in `.fit` format.
- With the CCD camera still covered, we collected 5 dark frames for each of the following exposure time intervals: 0.1 s, 1 s, 10 s and 100 s.
- The CCD camera was connected to the telescope in place of the eyepiece.
- A set of 10 flat-field frames was taken. As previously mentioned, a flat image is obtained by uniformly illuminating the CCD. This result can be achieved through various techniques in professional telescopes such as internal flat, dome flat, sky flat, or twilight flat. In our case, an illuminated white panel was placed in front of the telescope during image acquisition.
- Using the telescope's auto-tracking system, Deneb was pointed. 27 different frames were collected with different exposure times, from 0.01 seconds to 0.5 seconds. Short time intervals such these prevent this luminous star to saturate the camera.
- Following the same procedure, we also collected 36 images for Vega, attempting to remain in the same range of exposure times as Deneb.
- We then collected 5 images with 2 s of exposure for M45.
- Finally, we acquired 5 images with 5 s exposure time for NGC 869.

4 Data Reduction and Results

The data reduction was performed using Python scripts and specialized modules like `Ccdproc`, following the procedure described in Sec. 2.4.

4.1 Bias frames

Bias frames were used to evaluate the bias value and its associated uncertainty. Usually, starting from the set of initial bias frames, a *master bias* was computed as the mean or the median of such images. The histogram of the master bias frame provides a Gaussian distribution, where the peak position represents the average pixel intensity at the zero level and its standard deviation is related to the readout noise through Eq. 6.
In our case, the averaged master bias was preferred, since its standard deviation is lower than that obtained using the median (as shown in Fig. 5). Table 2 illustrates the results.

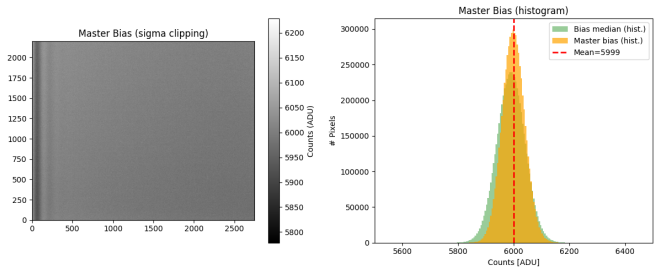

Figure 5: Master bias frame and counts distribution.

Frame Type	Mean(ADU)	Median(ADU)	StD. (ADU)
Bias	5999	5999	41

Table 2: Statistical properties of the bias frames. Values are in ADU. (StD. is the Standard Deviation).

Bias images must be taken during each night of observation, as they may vary depending on factors such as temperature or other hardware conditions. The next step involves subtracting the master bias from all the other images.

4.2 Flat-Field frames

Firstly, we subtracted the master bias to each of the initial flat frames. As for the bias frames, a *master flat* was computed as the mean of the bias-subtracted frames. The master flat was then normalized by dividing it by its mean value to avoid disproportionately reducing the scientific image. The normalized master flat is shown in Fig. 6 and its parameters are summarized in Tab. 3.
Before averaging the 10 flat images, extremely high counts per pixel (which are caused primarily by cosmic rays hits) were excluded using the *sigma clipping* method. This consists in discarding the data that deviate excessively from a certain reference value to eliminate the effect of spurious measurements on statistics. We chose the median as the typical value (it is more stable than the mean) and the MAD (Median-Absolute-Deviation) as the estimator of the deviation. We used a reasonable MAD of 3σ.

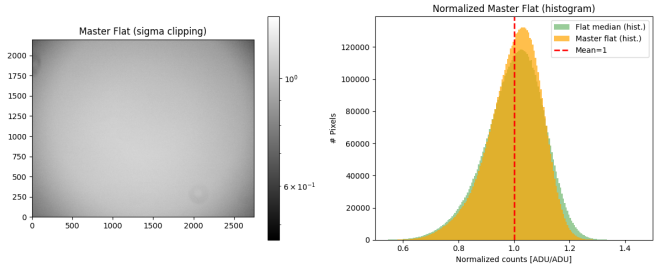

Figure 6: Normalized master flat frame and counts distribution.

Frame Type	Mean	Median	StD.
Flat	1.000	1.010	0.096

Table 3: Statistical properties of the normalized flat frame. Values are dimensionless because of the normalization.

Finally, using the `ccdmask` function from `ccdproc`, malfunctioning pixels (commonly referred to as *bad pixels*) were found and masked.

4.3 Dark current frames

Even though the CCD was cooled to minimize the dark current as much as possible, the effect of thermo-electrons should have been visible given that a non-professional camera with a basic camera cooling system was used.
We proceeded by bias-subtracting and flat-correcting (which means dividing the image by the normalized master flat) the dark frames. Then, the sets of 5 dark frames with the same exposure time were averaged to create 4 *master darks*. Table 4 and Fig. 8-10 provide the results of this process.

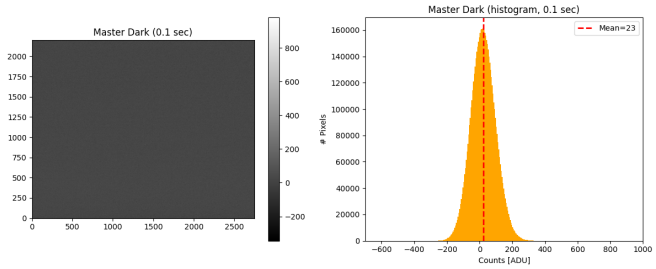

Figure 7: Master dark frame and counts distribution at 0.1 s exposure time.

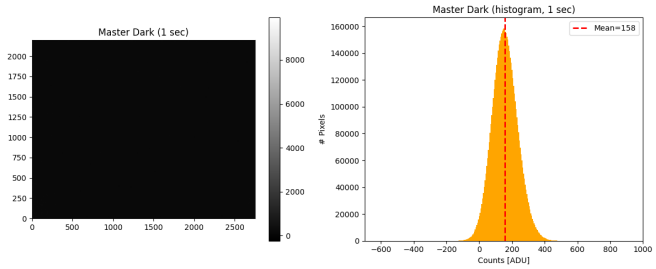

Figure 8: Master dark frame and counts distribution at 1 s exposure time.

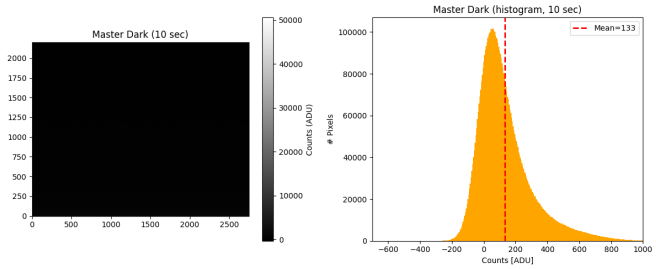

Figure 9: Master dark frame and counts distribution at 10 s exposure time.

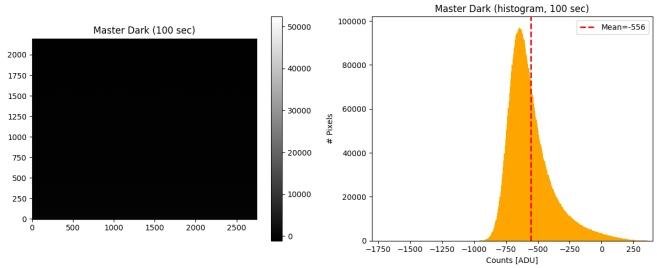

Figure 10: Master dark frame and counts distribution at 100 s exposure time.

Exp. Time(s)	Mean(ADU)	Median(ADU)	StD.(ADU)
0.1	23	21	76
1	158	155	78
10	133	96	176
100	-556	-596	209

Table 4: Statistical properties of the dark frames for different exposure times. Values are in ADU.

For reasons explained in Sec. 5, master dark frames were not suitable for image processing.
However, using the one with the highest exposure time we still tried to search for another unwanted feature in our images: hot pixels. These are pixels with high dark

current level that need to be masked in the scientific images. Their effect increases linearly with exposure time. We found 422 hot pixels.

4.4 Gain and Readout Noise

As introduced in Sec. 2.1.2, the gain is the amount of voltage required to produce 1 ADU. Since the digital number must be integer, the digitization process only accounts for electrons that are integer multiples of the gain [1]. The readout noise (RON) is the result of two different effects which combine casually. First of all, the analogical to digital conversion is not perfectly reproducible and so the final counts always carry an intrinsic uncertainty. Then the camera's electronics introduce spurious electrons into the entire process, causing unwanted random fluctuations in the resulting image.
It is possible to obtain a gain and readout noise estimation value by collecting 2 bias frames B_1, B_2 and 2 flat frames F_1, F_2.

$$\text{Gain} = \frac{(\overline{F}_1 + \overline{F}_2) - (\overline{B}_1 + \overline{B}_2)}{\sigma^2_{\overline{F}_1 - \overline{F}_2} - \sigma^2_{\overline{B}_1 - \overline{B}_2}} \tag{5}$$

$$\text{RON} = \frac{\text{Gain} \cdot \sigma_{\overline{B}_1 - \overline{B}_2}}{\sqrt{2}} \tag{6}$$

where $\overline{A}$ indicates the mean and σ_A the standard deviation of the count distribution for the image A. We computed gain and readout noise using every combination of flat and bias frames available. In Table 5, the values of these two quantities are given as the average of all estimations, with the uncertainties represented by their standard deviations. In Sec. 5

Parameter	Value	Uncertainty
Gain	0.027 e^-/ADU	0.009 e^-/ADU
Read-Out Noise (RON)	3.5 e^-	1.2 e^-

Table 5: Gain and read-out noise (RON) measurements, with associated uncertainties.

4.5 Photometry on calibrated images

4.5.1 Searching for the calibration constant C

We proceeded by calibrating the images of Deneb and Vega. Each one was bias-subtracted, flat-corrected and masked to hide bad pixels. Since the apparent magnitudes m_{ref} of these two stars are well known (1.25 for Deneb with a 0.04 variability, and 0.03 for Vega with 0.04 variability), the goal was to compute the calibration constant C from Eq. 3:

$$C = m_{ref} + 2.5 \log_{10}(R) \tag{7}$$

with $R = S - n_{pix}B$. Given the value of C, we could then get the magnitude of the stars in the Pleiades and NGC 869 clusters using the same relation.
Unfortunately, after processing, we had to discard the great majority of Deneb and Vega's frames. Some of the images were used, during the night of the observation, just to center the object in the field of view of the telescope before focusing. However, most of the actual scientific frames showed highly negative counts per pixel (<-1000 ADU in some cases) and would have significantly compromised the accuracy of our estimates if employed. Further discussion on the matter can be found in Sec. 5.
We were then forced to select the best image for each target: for Deneb we took a frame with 0.01 s exposure time and for Vega one with 0.05 s (such low exposure times were chosen during the observation in order to avoid saturating the two stars). The two processed images are show in Fig. 11, 12.

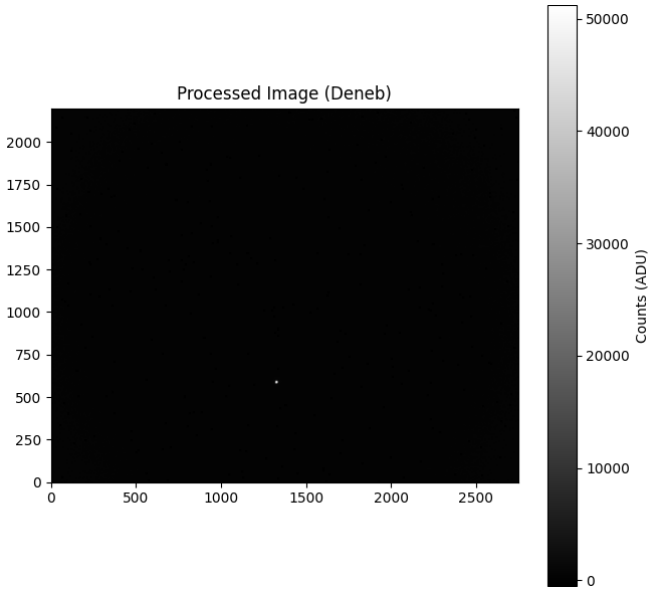

Figure 11: Processed image of Deneb.

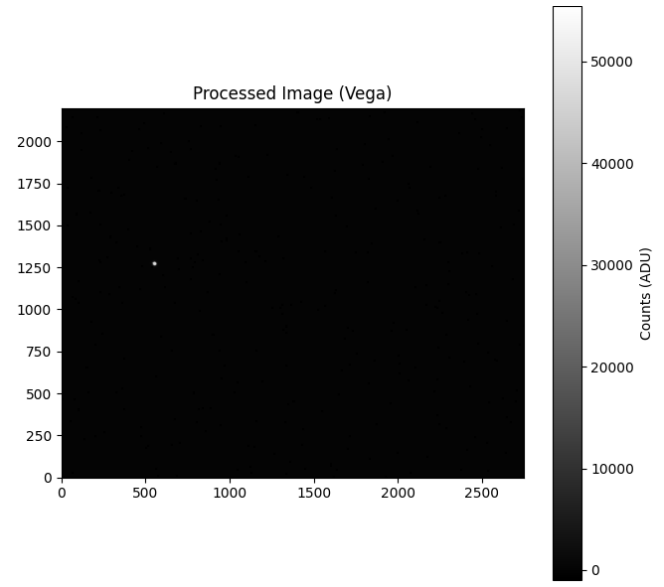

Figure 12: Processed image of Vega.

We proceeded estimating the uncertainty on the counts of each pixel using Eq. 18 in App. A.1. Then, using the `CircularAperture`, `Circular Annulus` and `ApertureStats` classes from the Python library `Photutils`, we were able to obtain the quantities S, B and n_{pix} in Eq. 7. In practice, the analysis was carried out as follows:

1. identified the stars in the `.fits` files using `DAOStarFinder` class from `Photutils`;

[1] For example, with a gain set to 5 e^-/ADU, if 20 electrons are measured in a certain pixel, then the count for such pixel will be equal to 4 ADU, but the same will be true with 24 electrons.

2. counted the number n_{pix} of pixels inside a circular aperture of chosen radius around the source;
3. summed the total counts S_t inside the circle;
4. computed the uncertainty on such sum starting from the uncertainty on each pixel;
5. computed the median [2] value B_t of the background in an annulus of chosen dimensions around the aperture (with its uncertainty).
6. computed $S = S_t/t_{exp}$ and $B = B_t/t_{exp}$ where t_{exp} denotes the exposure time of the image;
7. estimated C as in Eq. 7.

Table 6 summarizes the results of aperture photometry on Vega and Deneb.

Star	t_{exp}(s)	R(ADU·10^6)	C
Deneb	0.01	9.67 ± 0.36	21.21 ± 0.08
Vega	0.05	20.79 ± 0.42	21.58 ± 0.06

Table 6: Photometric measurements of Vega and Deneb using aperture photometry.

The uncertainty on the total counts was computed through `ApertureStats`. The uncertainty σ_C on C [3] was computed as the maximum propagated error as follows:

$$\sigma_c = \frac{2.5}{\ln(10)} \left(\frac{\sigma_{t_{exp}}}{t_{exp}} + \frac{\sigma_R}{R} \right) + \sigma_C \quad . \tag{8}$$

We assumed $\sigma_{t_{exp}}/t_{exp} << \sigma_R/R$ and used the variability of the magnitude of Vega and Deneb as $\sigma_{m_{ref}}$.
We also performed PSF Photometry on the selected images. This method consists of fitting a 2D function (a Gaussian in our case) for each detected source in the background - subtracted image and estimating the total counts by integrating such function over the area corresponding to the source in the CCD frame. This is automatically done by the class `ItertivePSFPhotometry` from `Photutils`, which also returns the residuals of the fit for each pixel. The value of C can then be found following the same process as before. The background was subtracted thanks to the `Background2D` class, also from `Photutils`. Fig. 17, 18 in App. A.2 show the residuals of the fit and Table 7 reports the results obtained with this method.

Star	t_{exp}(s)	R (ADU ·10^6)	C
Deneb	0.01	7.50 ± 0.02	20.95 ± 0.04
Vega	0.05	1.870 ± 0.001	21.46 ± 0.04

Table 7: Photometric measurements of Vega and Deneb using PSF photometry.

In this case, the error on R was calculated as the quadrature sum of the residuals within a square region of pixels around the star.
The final value of C was obtained by averaging the values derived solely from aperture photometry and propagating the maximum uncertainty. The reasons behind this choice are explained in Sec. 5.
In the end, we got $\mathbf{C = 21.40 \pm 0.07}$.
With PSF photometry measurements we would have obtained $C_{PSF} = 21.20 \pm 0.04$.

[2] We preferred the median over the average because it better accounts for the possible near sources around the star.
[3] From now on we will denote the uncertainty on a value a as σ_a.

4.5.2 Magnitude of stars in the Pleiades cluster

The images of M45 and NGC 869 were processed exactly with the same procedure adopted for Deneb and Vega: they were bias-subtracted, flat-corrected and masked for bad pixels.
Again, we had to discard many of them. In particular, none of the NGC 869 images were suitable for photometric analysis and only one from M45 was selected. A more detailed discussion of this issue is provided in Sec. 5. The chosen M45 image after processing is shown in Fig. 13.

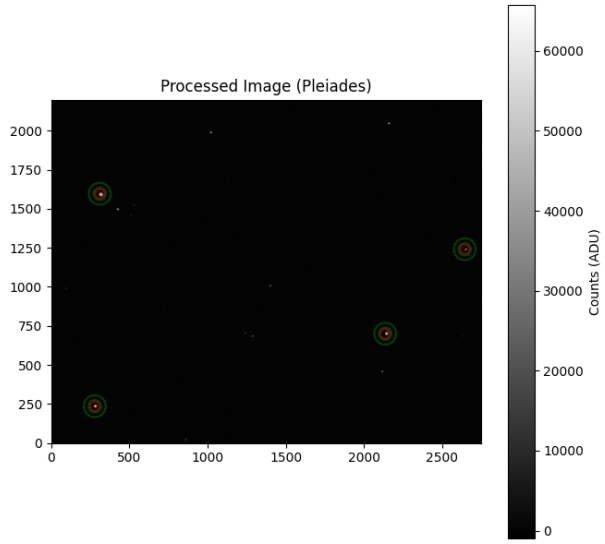

Figure 13: Processed image of M45. The circles highlight the targeted stars. In particular the green circle delimits the area used to estimate the star counts in aperture photometry, while the local background is evaluated in the red annulus.

Using `DAOStarFinder`, we selected the four most luminous stars in the M45 frame and performed aperture photometry, as previously explained. The names of the detected stars were identified by comparing the frame with an image of the well-known Pleiades cluster.
The magnitude m of the stars was found using Eq. 3 and the previously computed C value. The uncertainty σ_m is the maximum propagated error. Tab. 8 presents the photometric measurements using the aperture method, along with the expected magnitude of the targets.

Star	t_{exp} (s)	R (ADU ·10^6)	m	m_{ex}
Merope	2	13.17 ± 0.46	4.35 ± 0.11	4.14
Alcyone	2	22.6 ± 0.46	3.78 ± 0.09	2.85
Maia	2	14.67 ± 0.41	4.24 ± 0.10	3.87
Asterope II	2	5.32 ± 0.44	5.32 ± 0.16	6.43

Table 8: Photometric measurements of the four brightest stars in M45 using aperture photometry.

Finally, the computations were repeated using C_{PSF} as the calibration constant and estimating the luminosity of the 4 targets trough PSF photometry. Tab. 9 summarizes the results and Fig. 19 in App. A.2 shows the residuals of the PSF fit.

Star	t_{exp} (s)	R (ADU ·10^6)	m	m_{ex}
Merope	2	7.57 ± 0.41	4.76 ± 0.10	4.14
Alcyone	2	6.83 ± 0.02	4.87 ± 0.04	2.85
Maia	2	6.49 ± 0.02	4.92 ± 0.04	3.87
Asterope II	2	4.80 ± 0.02	5.25 ± 0.04	6.43

Table 9: Photometric measurements of the four brightest stars in M45 using PSF photometry.

5 Discussion

5.1 CCD characterization problems

From Fig. 7 - 10 one can easily see how dark frames were practically unusable for image processing, except maybe for the one with 1 s exposure. First of all, after bias-subtraction and flat-correction a great fraction of the pixels had highly negative counts. For the low exposure dark frames (0.1 s and 1 s) this can be explained by the fact that nearly all pixels are basically at bias level, since thermal noise increases with time and no photoelectrons can be detected. Therefore, given the uncertainty on the bias counts per pixel, subtracting the master bias could produce some negative counts. This is shown in the 0.1 s master dark histogram in Fig. 7, where the Gaussian distribution is nearly centered on zero, since the time interval is so small that very few thermal electrons were produced in the camera. However, Fig. 9, 10 show a non-Gaussian distribution with a high percentage of negative counts, particularly in the 100 s exposed one. These problems probably arose from technical imperfections in the CCD camera itself or from incorrect settings in the software used to save the dark frames.
Even though dark frames couldn't be subtracted during image processing, this inconvenience shouldn't have affected our results in a significant way: our scientific images had low exposure times (from 0.01 s to 5 s) and the sources that we were able to detect had high counts per pixel ($\sim 10^5$ ADU [4]), which means that the disturbance of the thermal noise should have been minimal.
To emphasize the reason why dark frames had to be discarded, Fig. 14 shows how the mean value of the dark current varies with exposure time according to our data. The relation between these two quantities should be linear, but fitting our measurements we found a negative proportionality constant which does not have any physical sense.
The search for hot pixels on such master dark frames was likely very inaccurate, and we preferred not to mask the 422 that were actually found. Again, this should not have compromised our results since the total number of pixels in the camera was above $6 \cdot 10^6$.
Note that in the case of the master flat the non-Gaussian distribution of pixel values may be attributed to dust on the telescope's mirror (as visible in Fig. 6) and to intrinsic pixel-to-pixel sensitivity variations across the CCD sensor. However, even the flat frames themselves might not have been sufficiently accurate, as the panels used during their acquisition were not uniformly illuminated with enough precision.
A strong indicator of these inaccuracies is the measured gain of the CCD, which appears unrealistically low since typical values are expected to lie within the range of 1 to 10 e^-/ADU. All of these observations suggest that our measurements (even bias frames) were strongly affected by systematic errors caused by several factors such as:

- probable improper configuration of the image saving software;
- technical limitations in the CCD camera (e.g problems in the A/D conversion system, pixel sensitivity)
- inadequate cooling of the CCD camera;
- human errors in the dark and flat frames taking procedure

[4] Assuming that the first two master dark frames were accurate, at 1 s exposure we would have had a thermal noise of $\sim 10^2$ ADU.

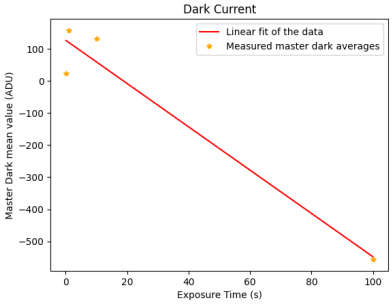

Figure 14: Wrongful relation between average dark current and exposure time according to our data. The slope of the fit is ≈ -7 (physically it should clearly be a positive number) and the intercept is ≈ 127 (ideally it should be zero since no dark current can be observed at 0 s exposure time).

5.2 Image processing issues

The severe problems affecting the calibration frames are only one of the possible reasons for the discrepancy between the results in Tab. 8, 9 and the expected magnitudes of the Pleiades cluster's stars.
Initially, observations were aimed to acquire a large number of images for Deneb and Vega, enabling a more robust determination of C through statistical analysis. However, after processing, many of the Vega's images displayed a background similar to the one shown in Fig. 15: high inhomogeneity and more importantly the presence of negative counts caused such frames to be discarded.

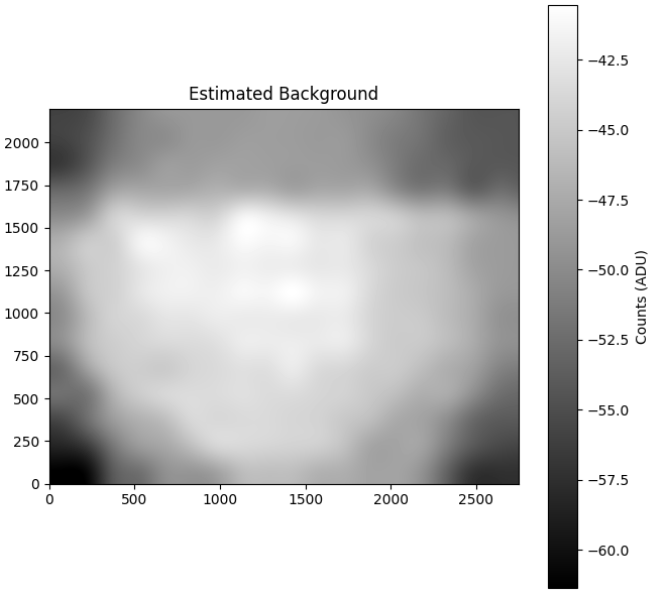

Figure 15: Background estimated through the `Background2D` class on a processed image of Vega. Note how nearly all pixels have counts of about -50 ADU, which does not have any physical meaning. One might argue that the exposure time of the image was so low (0.01 s) that (except for the small area occupied by star) the frame should all be practically at zero level, and thus a -50 ADU count could be accepted without grave consequences on statistic for luminous sources. However, since the observations were carried out in an urban area, the sky level itself must have been sufficiently high to shift the image significantly above the bias level. This indicates that this frame is too affected by systematic errors to be employed in photometric analysis.

With the same criteria, NGC 869's images (one of which is reported in Fig. 16 along with its estimated background) were deemed unusable.

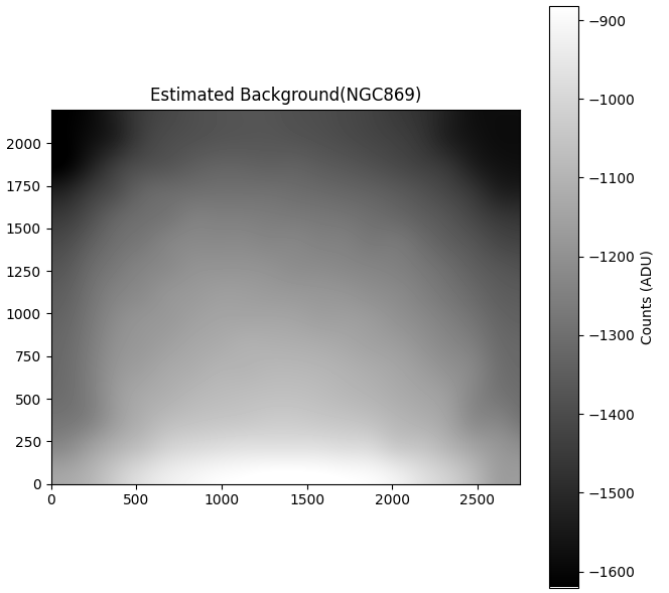

Figure 16: Background estimated through the `Background2D` class on a processed image of NGC 869. Note how nearly all pixels have counts of about -1000 ADU, which does not have any physical meaning.

As previously mentioned, we also preferred working with the total counts per star measured with aperture photometry technique instead of the one inferred through PSF photometry. After many tries at tuning the initial parameters for the 2D-Gaussian fitter function, the residuals for the M45 image were still higher than expected and the resulting total counts were systematically lower than the value derived from aperture photometry. Comparing Tab. 9 and 8, it becomes clear that PSF photometry returns a worse estimate for the real magnitude of the targets. The reasons for such inaccuracy could reside in the fact that the PSF profile may not be represented by a 2D-Gaussian. Moreover, the low quality of the calibration frames undoubtedly affected the scientific images, distorting the PSF.
It should also be mentioned that no professional telescope or CCD camera was used for the observations, which limited the achievable image quality in the first place.

6 Conclusion

The limitations given by systematic errors and instrumentation issues did not allow us to perform our measurements in an accurate way. However, a coherent methodology for performing aperture and PSF photometry using dedicated Python modules was developed, and the CCD camera was characterized as well as the calibration frames permitted. The calibration constant was evaluated at $C = 21.40 \pm 0.07$, and the magnitude of the four most luminous stars in the M45 cluster were computed (Tab. 8). Neither aperture nor PSF photometry was performed on NGC 869 images. Observations carried out with refined instruments and procedures could likely have improved the reliability of the results.

A Appendix

A.1 Computing the uncertainty on the counts of each pixel

Let us call $\sigma^2_{r,p}$ the uncertainty on the value of a preprocessed pixel, given by

$$\sigma^2_{r,p}[x,y] = \sigma^2_r + \sigma^2_{\zeta,e} + \sigma^2_{d,e} + \sigma^2_L r^2 + \sigma^2_f (r - d_e - \zeta_e)^2, \quad (9)$$

and $\sigma^2_{b,e}$ the uncertainty on the estimated background. It is possible to split the pixel count in several components as follows:

$$r_p[x,y] = \frac{1}{f[x,y]}\{L(r[x,y])r[x,y] - d_e[x,y] - \zeta_e[x,y]\} \quad (10)$$

where $f[x,y]$ is the normalized response of the flat field, $d_e[x,y]$ is estimated dark count, $L(r[x,y])$ is the linearity correction and $\zeta_e[x,y]$ is the bias level. All these quantities are expressed in electrons (not in ADU). Assuming that the uncertainties on each of the variables are not correlated, the *processed pixel variance* is provided by

$$\sigma^2_{r,p}[x,y] = \sigma^2_r \frac{L^2}{f^2} + \sigma^2_{d,e}\frac{1}{f^2} + \sigma^2_{\zeta,e}\frac{1}{f^2} + \sigma^2_L \frac{r^2}{f^2} + \sigma^2_f \left\{\frac{Lr - d_e - \zeta_e}{f^2}\right\}^2 .$$

It is possible to assume that $f \simeq 1$ e $L \simeq 1$, so

$$\sigma^2_{r,p}[x,y] = \sigma^2_r + \sigma^2_{\zeta,e} + \sigma^2_{d,e} + \sigma^2_L r^2 + \sigma^2_f (r - d_e - \zeta_e)^2 \quad . \quad (11)$$

On the other hand, the count value of an unprocessed pixel is given by

$$r[x,y] = r'[x,y] + \zeta[x,y] = n[x,y] + b[x,y] + d[x,y] + \zeta[x,y], \quad (12)$$

where n is the contribution of the signal coming from the targeted source, b the background, d the dark and ζ the bias (all expressed in electrons). The variance of the rough pixel is:

$$\sigma^2_r[x,y] = \sigma^2_{r'} + \sigma^2_\zeta = r' + \rho^2 \quad . \quad (13)$$

The variance of the pixel response, $r'[x,y]$ is equivalent to its mean because the response follows a poissonian distribution. Regarding the bias variance ρ^2, we can analyze two different components:

$$\rho^2 = \sigma^2_{read} + \sigma^2_{digit} \quad . \quad (14)$$

σ^2_{read} is the reading error, the uncertainty in the zero-level signal originating from the output amplifier; σ^2_{digit} is the quantization error, the uncertainty that arises when the ADC circuit rounds the analog signal to the nearest integer. So, after the estimation of the d and b values, one can write

$$\sigma^2_r[x,y] \approx n + b_e + d_e + \rho^2 \quad . \quad (15)$$

We now consider the second term in Eq. 11, which represents the squared uncertainty of the estimated bias level. If p_z bias frames are acquired, the minimum variance of the mean of the p_z bias values at a given pixel $[x,y]$ is given by:

$$\sigma^2_{\zeta,e} = \frac{\rho^2}{p_z}. \quad (16)$$

The third term is the variance of the estimated dark counts. If the estimate is obtained as the mean of p_d

dark frames, each taken with the same exposure time as the science image, then the variance of the mean is given by:

$$\sigma^2_{d,e} = \frac{1}{p_d}\left\{d_e + \left(1 + \frac{1}{p_z}\right)\rho^2\right\} \quad . \tag{17}$$

The second term arises from the fact that the dark frames are processed by subtracting the estimated bias level. The fourth contribution $\sigma^2_L r^2$ to the noise is the variance associated with the linearity correction, scaled by the square of the pixel value. The response of a CCD is not always perfectly linear with respect to the incoming light. A linearity correction is applied. The fifth contribution $\sigma^2_f (n+b)^2$ arises from the uncertainty in the normalized flat field. In the ideal case, σ^2_f approaches $(n_f[x,y])^{-1}$, where $n_f[x,y]$ is the total number of photoelectrons counted at the pixel position $[x,y]$ over all calibration exposures collected for the flat field. Therefore, this uncertainty can be reduced simply by accumulating a sufficient number of calibration frames.
Finally, by summing all contributions, the variance for a *single preprocessed pixel* is given by:

$$\sigma^2_{r,p}[x,y] = n + b_e + a_d(d_e + a_z\rho^2) + \sigma^2_L r^2 + \sigma^2_f (n+b_e)^2 \tag{18}$$

with $a_d = 1 + \frac{1}{p_d}$ and $a_z = \frac{1}{p_z}$.

A.2 Figures

Fig. 20 shows the processed images of NGc 869 corresponding to the background in Fig. 16 that were discarded. Fig. 17-19 were mentioned in the previous sections.

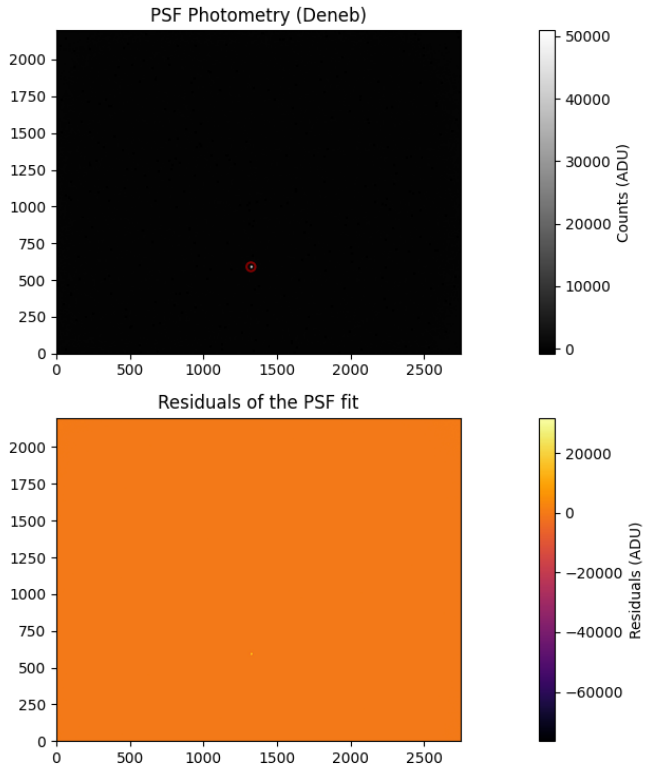

Figure 17: PSF photometry on Deneb. *Above*: star found through `DaoStarfinder` *Below*: residuals of the PSF fit.

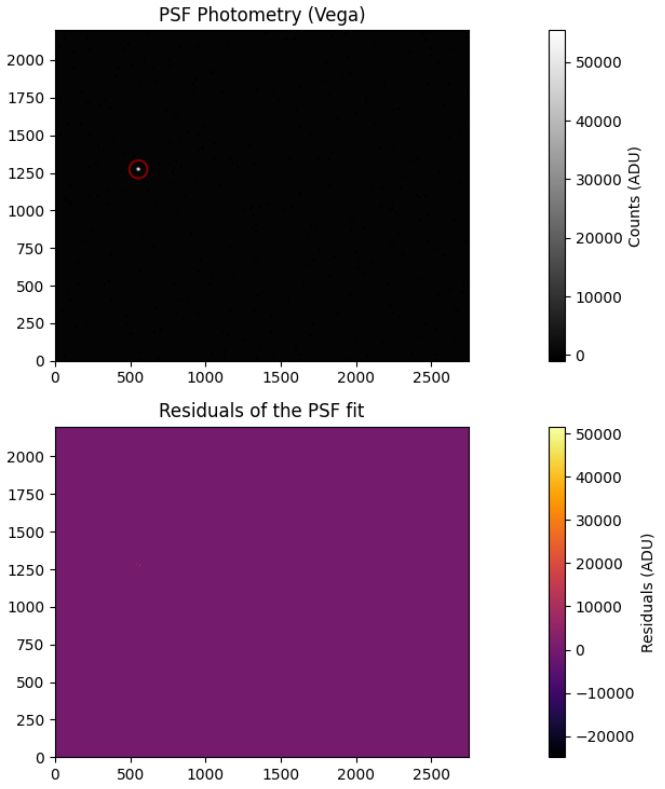

Figure 18: PSF photometry on Vega. *Above*: star found through `DaoStarfinder` *Below*: residuals of the PSF fit.

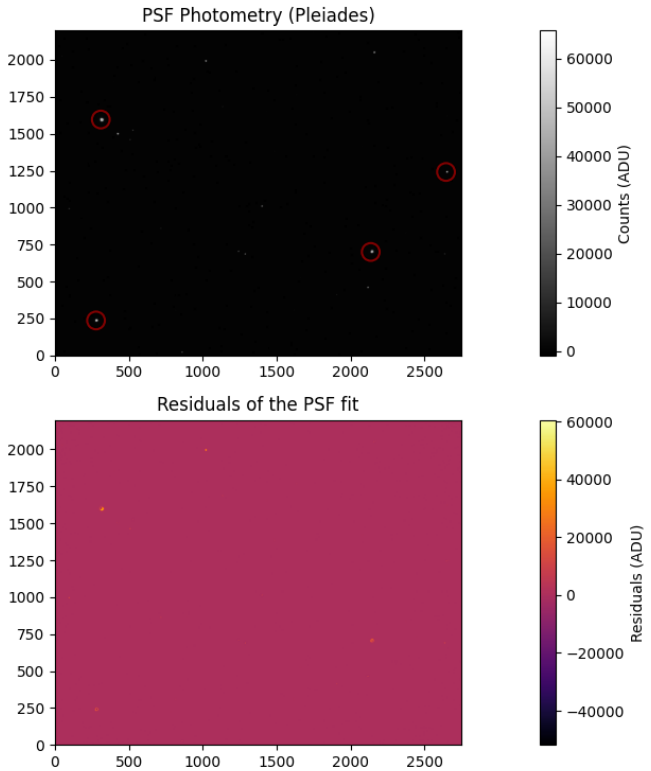

Figure 19: PSF photometry on 4 stars in M45. *Above*: stars found through `DaoStarfinder` *Below*: residuals of the PSF fit.

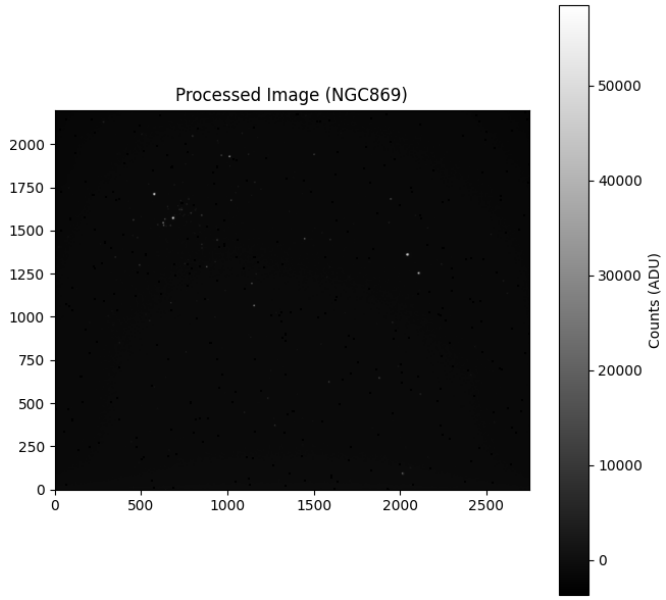

Figure 20: *Above*: Processed image of NGC 869.

References

[1] URL: https://photutils.readthedocs.io/en/stable/user_guide/index.html.

[2] *CCD Data Reduction Guide*. URL: https://www.astropy.org/ccd-reduction-and-photometry-guide/v/dev/notebooks/00-00-Preface.html.

[3] Stefano Ciroi and Valentina Cracco. *Dispense di laboratorio di astronomia*. Dipartimento di Fisica e Astronomia, Università degli Studi di Padova, 2015.

[4] Enrico Maria Corsini. *Astrofisica 1*. Lectures given in the Bachelor's degree program in Astronomy, University of Padua. Presentation slides. 2023.